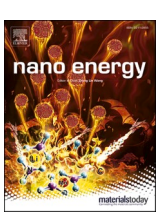
ELSEVIER

Contents lists available at ScienceDirect

Nano Energy

journal homepage: www.elsevier.com/locate/nanoen





Bulk heterojunction perovskite solar cells incorporated with p-type low optical gap conjugated polymers

Lening Shen a, Tao Zhu a, Xinwen Zhang b, Keven Gong c, 1, He Wang b, Xiong Gong a, *

- ^a School of Polymer Science and Polymer Engineering, The University of Akron, Akron, OH 44325, USA
- ^b Department of Physics, University of Miami, Coral Gables, FL 33146, USA
- ^c Western Reserve Academy, Hudson, OH

ARTICLE INFO

Keywords:

Perovskite solar cells Bulk heterojunction device structure Low optical gap conjugated polymer Efficiency Stability and photocurrent hysteresis

ABSTRACT

Perovskite solar cells (PSCs) as alternative cost-effective solar technology have drawn great concentrations in both academic and industrial sectors in the past years. Through the film morphological manipulation of perovskite photoactive layers and generic interfacial engineering, efficient PSCs have been reported. However, intrinsic unbalanced charge transport within the perovskite photoactive layer, which restricted further boost device performance of PSCs, was not fully addressed. In this study, we report high-performance bulk heterojunction (BHJ) PSCs based on the composites composed of n-type $Cs_{0.15}FA_{0.85}PbI_3$ (where FA is formamidinium, $HC(NH_2)_2$) incorporated with p-type low optical gap conjugated polymer. Compared to pristine $Cs_{0.15}FA_{0.85}PbI_3$ thin film, the BHJ composite thin film possesses enhanced and balanced charge carrier mobilities, enlarged crystal sizes, and suppressed non-radiation charge carrier recombination. Most importantly, a photo-induced charge transfer occurs within the BHJ composite thin film. As a result, the BHJ PSCs exhibit a power conversion efficiency (PCE) of 21.08%. In addition, un-encapsulated BHJ PSCs possess remarkably enhanced stability (as they retain 80% of their initial PCE after ~ 200 days in ambient conditions) and diminished photocurrent hysteresis index of 0.012) compared to those based on pristine $Cs_{0.15}FA_{0.85}PbI_3$ thin film. All these results demonstrate that the PSCs with a BHJ device structure are one of the facile ways to approach high-performance PSCs.

1. Introduction

Perovskite solar cells (PSCs) have drawn great attention in both academic and industrial sectors in the past decade [1–11]. Through the film morphological manipulation of perovskite photoactive layers and generic interfacial engineering of the electron and/or hole extraction layers (EEL and HEL), over 25% power conversion efficiencies (PCEs) were reported from PSCs with a conventional device structure [12]. While impressive device performance has been reported, the intrinsic unbalanced charge transport within perovskite photoactive layers is a limiting factor for further boosting device performance [13,14]. Many effects have been paid to address this bottleneck problem for boosting device performance [12–25]. For example, high-temperature sintered EEL was typically used in the PSCs with a mesoscopic device structure [12,15] and the EEL with decent electron mobility was also used in the PSCs with a planar device structure [16]. To further address unbalanced

charge transport within perovskite photoactive layers, our group first reported the PSCs with a bulk heterojunction (BHJ) device structure, where solution-processed perovskites were mixed with the n-type electron acceptors, such as fullerene derivatives, inorganic nanoparticles, and low optical gap conjugated organic molecules [17,18]. Further studies demonstrated that the PSCs based on BHJ composite thin film possessed improved charge carrier extraction efficiency and suppressed photocurrent hysteresis compared to those based on pristine perovskite thin film [17–24]. All these earlier studies were focused on p-type perovskites incorporated with n-type electron acceptors [17,19,25]; whereas, n-type perovskites incorporated with p-type electron donors for balancing charge transport of perovskite photoactive layers used for boosting device performance was rarely reported so far.

In this study, we report high-performance BHJ PSCs based on n-type $Cs_{0.15}FA_{0.85}PbI_3$ (where FA is formamidinium. $HC(NH_2)_2$) incorporated with p-type low optical gap conjugated polymer, poly(5,7-bis(4-

E-mail addresses: hewang@miami.edu (H. Wang), xgong@uakron.edu (X. Gong).

^{*} Corresponding authors.

 $^{^{1}}$ High-school student from Western Reserve Academy working in summer.

decanyl-2-thienyl)-thieno(3,4-b)diathiazole-thiophene-2,5) (PDDTT) [26]. Compared to pristine $Cs_{0.15}FA_{0.85}PbI_3$ thin film, the $Cs_{0.15}FA_{0.85}PbI_3$:PDDTT BHJ composite thin film possess enhanced and balanced charge carrier mobilities, enlarged crystal sizes, and suppressed non-radiation charge carrier recombination. More importantly, a photo-induced charge transfer occurs within the $Cs_{0.15}FA_{0.85}PbI_3$: PDDTT BHJ composite thin film. Therefore, the PSCs based on the $Cs_{0.15}FA_{0.85}PbI_3$:PDDTT BHJ composite thin film exhibit enhanced power conversion efficiency, boosted stability, and suppressed photocurrent hysteresis compared to those based on pristine $Cs_{0.15}FA_{0.85}PbI_3$ thin film.

2. Results and discussion

 $Cs_{0.15}FA_{0.85}PbI_3$ is a narrow bandgap (1.47 eV) perovskite [27,28], and has already become a major research avenue in the development of efficient and stable PSCs due to their stabilized phase and processibility in green solvents [29,30]. However, unbalanced charge transport within $Cs_{0.15}FA_{0.85}PbI_3$ thin film, which is similar to other perovskites [25,31], restricts device performance of PSCs [27–30].

To balance charge transport, consequently, boost the device performance of the PSCs based on Cs_{0.15}FA_{0.85}PbI₃ thin film, we utilize Cs_{0.15}FA_{0.85}PbI₃ incorporated with p-type, low optical gap conjugated polymer, PDDTT, to form the Cs_{0.15}FA_{0.85}PbI₃:PDDTT BHJ composite thin film as the photoactive layer. PDDTT (molecular structure as shown in the insert of Fig. 1a) is selected as the electron donor to balance charge transport since it possesses decent charge carrier mobility [26]. Fig. 1a shows the UV-visible absorption spectra of Cs_{0.15}FA_{0.85}PbI₃ thin film, the Cs_{0.15}FA_{0.85}PbI₃:PDDTT BHJ composite thin film, and PDDTT thin film. PDDTT exhibits strong absorption from the UV-visible to the near-infrared (NIR) region, which could serve as a complementary absorber for Cs_{0.15}FA_{0.85}PbI₃ to enhance the short-circuit current (J_{SC}) of the PSCs based on the Cs_{0.15}FA_{0.85}PbI₃:PDDTT BHJ composite thin film. Compared to pristine $Cs_{0.15}FA_{0.85}PbI_3$ thin film, the Cs_{0.15}FA_{0.85}PbI₃:PDDTT BHJ composite thin film has an enhanced absorption intensity ranging from 600 nm to 800 nm, which is ascribed to the contribution of PDDTT. However, the Cs_{0.15}FA_{0.85}PbI₃:PDDTT BHJ composite thin film exhibit negligible absorption in the NIR region. which is probably originated from a little PDDTT mixed with Cs_{0.15}FA_{0.85}PbI₃ since PDDTT has poor solubility in the dimethyl sulfoxide: N, N-dimethylformamide (DMSO:DMF) mixed solvent, which was typically used for the preparation of Cs_{0.15}FA_{0.85}PbI₃ solution. Nevertheless, enhanced absorption ranging from 600 nm to 800 nm could contribute to J_{SC} for the PSCs based on the Cs_{0.15}FA_{0.85}PbI₃:PDDTT BHJ composite thin film.

To verify the hypothesis that p-type PDDTT could balance charge transport of the $Cs_{0.15}FA_{0.85}PbI_3$:PDDTT BHJ composite thin film with respect to pristine $Cs_{0.15}FA_{0.85}PbI_3$ thin film, charge carrier mobilities of

two different thin films are investigated using the space-charge-limitedcurrent (SCLC) method based on the Mott-Gurney model [32,33]. Fig. 1b displays the current versus voltage (I-V) characteristics of the hole-only and electron-only diodes based on either pristine Cs_{0.15}FA_{0.85}PbI₃ thin film or the Cs_{0.15}FA_{0.85}PbI₃:PDDTT BHJ composite thin film. At low voltage, the I-V curves conform the Ohm's law in both Ohmic and the trap-filling regions. The SCLC is described as $J = \frac{8}{9} \varepsilon_0 \varepsilon \mu \frac{V^2}{I^3}$ (where μ is the mobility of charge carriers, V is the applied voltage and Lis the thickness of the active layer, ε_0 is the permittivity of free space of $8.55 \times 10^{-12} \, \mathrm{F m^{-1}}$, ε is the relative dielectric constant of active layer material). Based on the capacitor versus frequency (C-F) characteristics (Fig. S1) of the diodes fabricated by either pristine $Cs_{0.15}FA_{0.85}PbI_3$ thin film and the Cs_{0.15}FA_{0.85}PbI₃:PDDTT BHJ composite thin film, ε of 29.39 and 38.66 are calculated for pristine $Cs_{0.15}FA_{0.85}PbI_3$ thin film and the Cs_{0.15}FA_{0.85}PbI₃:PDDTT BHJ composite thin film, respectively. Thus, the hole and electron mobilities of pristine Cs_{0.15}FA_{0.85}PbI₃ thin film are calculated to be $4.76 \times 10^{-4} \text{ cm}^2 \text{V}^{-1} \text{s}^{-1}$ and $5.03 \times 10^{-3} \text{ cm}^2 \text{ V}^{-1} \text{ s}^{-1}$, which results in a μ_h/μ_e of 0.10. These results indicate that pristine Cs_{0.15}FA_{0.85}PbI₃ thin film is an n-type semiconductor and its charge transport is unbalanced. Whereas the hole and electron mobilities are calculated to be 4.05 \times 10^{-3} cm 2 V^{-1} s^{-1} and 1.05 \times 10^{-2} cm 2 V^{-1} s^{-1} for the Cs_{0.15}FA_{0.85}PbI₃:PDDTT BHJ composite thin film, which results in a μ_h/μ_e of 0.38. These results indicate that both electron and hole mobilities are enhanced and the charge transport within the Cs_{0.15}FA_{0.85}PbI₃:PDDTT BHJ composite thin film is more balanced than that of pristine Cs_{0.15}FA_{0.85}PbI₃ thin film. As a result, the PSCs based on the Cs_{0.15}FA_{0.85}PbI_{3:}PDDTT BHJ composite thin film is expected to exhibit boosted JSC.

Fig. 2a-c presents the grazing-incidence wide-angle x-ray scattering (GIWAXS) profiles of pristine Cs_{0.15}FA_{0.85}PbI₃ thin film and the Cs_{0.15}FA_{0.85}PbI₃:PDDTT BHJ composite thin films incorporated with different concentrations of PDDTT. Pristine Cs_{0.15}FA_{0.85}PbI₃ thin film possesses the (011), (111), and (210) planes, which corresponds to the tetragonal crystal structure. The $Cs_{0.15}FA_{0.85}PbI_3$:PDDTT BHJ composite thin films possess the (011), (111), and (210) planes, but with different reflection intensities. As the concentration of PDDTT is at 0.02 mg/mL, the reflection intensities of the (011), (111), and (210) planes are reduced and the (100) and (200) planes, which correspond to the cubic crystal structure, are appeared. As the concentration of PDDTT is at 0.08 mg/mL, the reflection intensities of the (011), (111), and (210) planes are increased but the reflection intensities of the (100) and (200) planes are decreased. These results demonstrate that the Cs_{0.15}FA_{0.85}PbI₃:PDDTT BHJ composite thin films have both tetragonal and cubic crystal structures, and their crystal structures are affected by

Fig. 2d displays the 1D GIWAXS profiles (the out-of-plane direction, incident angle of 0.14°), which are extracted from the 2D GIWAXS

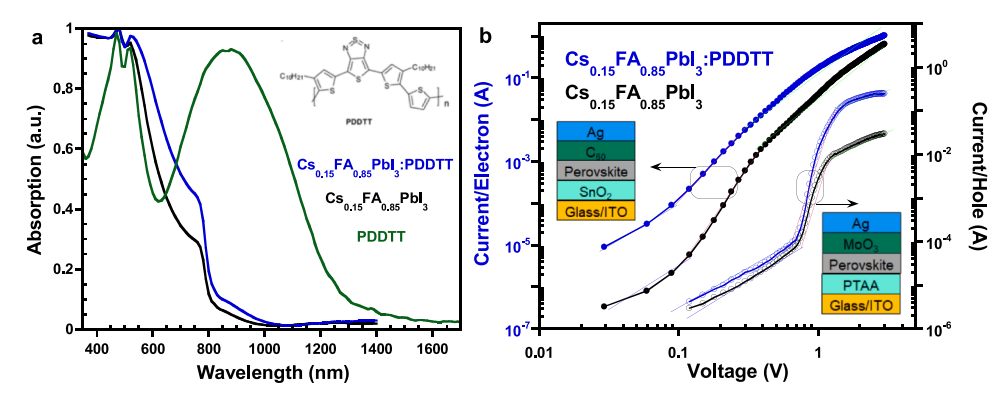


Fig. 1. a) The absorption spectra of pristine $Cs_{0.15}FA_{0.85}PbI_3$ and PDDTT thin films, and the $Cs_{0.15}FA_{0.85}PbI_3$:PDDTT BHJ composite thin film, insert is the molecular structure of PDDTTT, b) the I-V characteristics of the hole-only and the electron-only diodes based on pristine $Cs_{0.15}FA_{0.85}PbI_3$ thin film and the $Cs_{0.15}FA_{0.85}PbI_3$: PDDTT BHJ composite thin film, insert are the device structures of the hole-only and electron-only diodes.

L. Shen et al. Nano Energy 93 (2022) 106907

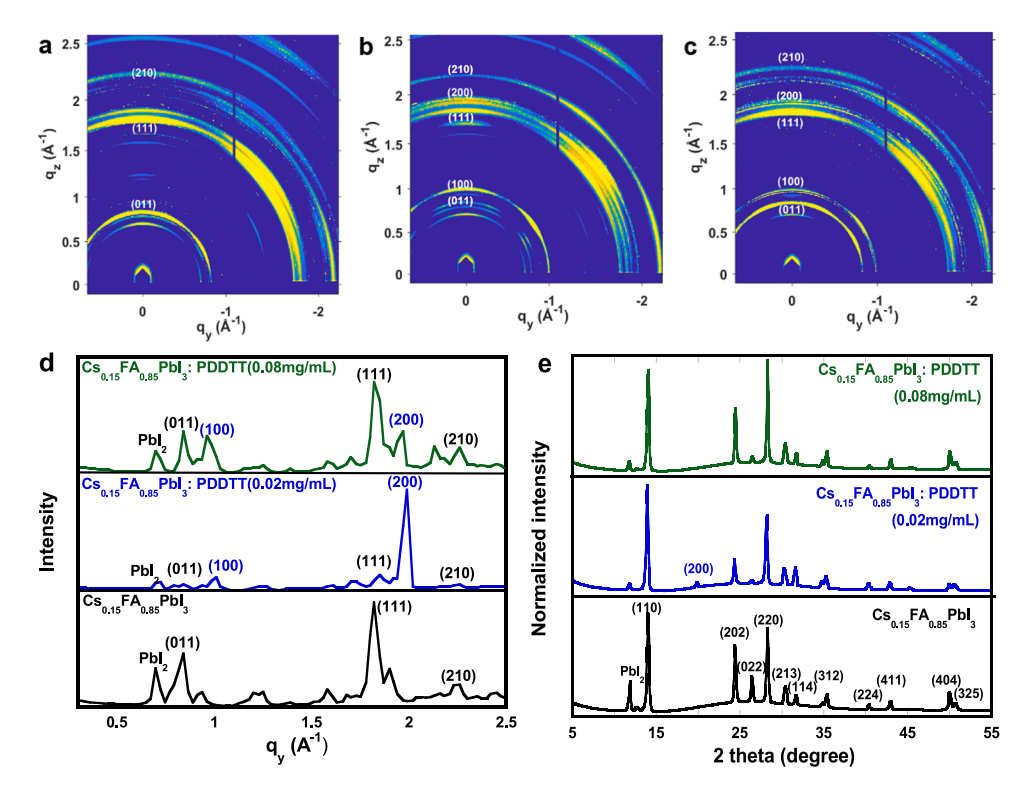


Fig. 2. The GIWAXS profiles of a) pristine $Cs_{0.15}FA_{0.85}PbI_3$ thin film and the $Cs_{0.15}FA_{0.85}PbI_3$:PDDTT BHJ composite thin films incorporated with b) 0.02 mg/mL of PDDTT and c) 0.08 mg/mL of PDDTT, d) the 1D GIWAXS line profiles extracted from (a–c) (the out-of-plane direction, incident angle of 0.14°), and e) the XRD patterns of pristine $Cs_{0.15}FA_{0.85}PbI_3$ thin film and the $Cs_{0.15}FA_{0.85}PbI_3$:PDDTT BHJ composite thin films.

profiles. Pristine Cs_{0.15}FA_{0.85}PbI₃ thin film possesses the (011), (111), and (210) planes, which further confirm that pristine Cs_{0.15}FA_{0.85}PbI₃ thin film possesses the tetragonal crystal structure. Compared to pristine Cs_{0.15}FA_{0.85}PbI₃ thin film, new peaks of the (100) and (200) planes presented in the Cs_{0.15}FA_{0.85}PbI₃:PDDTT BHJ composite thin film incorporated with 0.02 mg/mL of PDDTT further indicate that some of the tetragonal crystal structure is tuned to the cubic crystal structure. However, decreased reflection intensities of the (100) and (200) planes and increased reflection intensities of the (011), (111), and (210) planes are observed from the Cs_{0.15}FA_{0.85}PbI₃:PDDTT BHJ composite thin film incorporated with 0.08 mg/mL of PDDTT. Such changes in the reflection intensities are probably ascribed to PDDTT, which occurs the grain boundary of Cs_{0.15}FA_{0.85}PbI₃ [17,19]. Nevertheless, the cubic crystal structure observed from the Cs_{0.15}FA_{0.85}PbI₃:PDDTT BHJ composite thin films implies that the PSCs based on the $Cs_{0.15}FA_{0.85}PbI_3$:PDDTT BHJ composite thin films exhibit boosted J_{SC} since the perovskites with a cubic crystal structure have superior electronic properties than those with a tetragonal crystal structure [6]. In addition, the PbI2 plan is presented within 1D GIWAXS profiles. The appearance of PbI2 is originated from the effect of the antisolvent treatment [30]. However, reduced peak intensities of PbI2 observed from the Cs_{0.15}FA_{0.85}PbI3: PDDTT BHJ composite thin films suggest that the counterions (Pb²⁺ and Γ) are suppressed, which would result in reduced photocurrent hysteresis for the PSCs based on the Cs_{0.15}FA_{0.85}PbI₃:PDDTT BHJ composite thin film [34].

The x-ray diffraction (XRD) patterns of pristine $Cs_{0.15}FA_{0.85}PbI_3$ thin film and the $Cs_{0.15}FA_{0.85}PbI_3$:PDDTT BHJ composite thin films are shown in Fig. 2e. The (110) and (220) planes at the peaks of 2θ of $\sim 14^\circ$ and $\sim 28^\circ$, respectively, demonstrate that pristine $Cs_{0.15}FA_{0.85}PbI_3$ thin film possesses the tetragonal (I4/mcm) crystal structure. The (200) plane observed within the $Cs_{0.15}FA_{0.85}PbI_3$:PDDTT BHJ composite thin film incorporated with 0.02 mg/mL of PDDTT indicates that partial tetragonal structure is tuned to the cubic structure. These observations are in good agreement with the GIWAXS results. However, the (200) plane,

corresponding to the cubic crystal structure, is disappeared in the $Cs_{0.15}FA_{0.85}PbI_3:PDDTT$ BHJ composite thin film incorporated with 0.08 mg/mL of PDDTT, indicating that the tetragonal crystal structure is dominated. All these results further demonstrate that PDDTT affects the crystal structure of the $Cs_{0.15}FA_{0.85}PbI_3:PDDTT$ BHJ composite thin films. Thus, the $Cs_{0.15}FA_{0.85}PbI_3:PDDTT$ BHJ composite thin film is expected to exhibit better photovoltaic properties compared to that of pristine $Cs_{0.15}FA_{0.85}PbI_3$ thin film.

The photovoltaic properties of the Cs_{0.15}FA_{0.85}PbI_{3:}PDDTT BHJ composite thin film are studied through the evaluation of the device performance of the PSCs with a device architecture as shown in Fig. 3a, where ITO is indium tin oxide and acts as the anode, PTAA is poly-[bis(4phenyl)(2,4,6-trimethylphenyl)amine] and is used as the HEL, C₆₀ acts as the EEL and the hole-block layer (HBL) as well, and BCP is bathocuproine and acts as an addition HBL, Al is aluminum and acts as the cathode, respectively. Fig. 3b displays the lowest unoccupied molecular orbital (LUMO) and highest occupied molecular orbital (HOMO) energy levels of PTTA, Cs_{0.15}FA_{0.85}PbI₃, PDDTT, C₆₀, and BCP, and the work functions of ITO and Al electrodes. The HOMO offset between PDDTT and Cs_{0.15}FA_{0.85}PbI₃ is 0.7 eV, which is larger than the exciton binding energy of Cs_{0.15}FA_{0.85}PbI₃ [26,30], indicating that the separated holes within the Cs_{0.15}FA_{0.85}PbI₃:PDDTT BHJ composite thin film can be easily transported to PDDTT electron donor layer and further collected by the ITO anode. Negligible LUMO offset between PDDTT and Cs_{0.15}FA_{0.85}PbI₃ indicates that the separated electrons can be easily transported to the low energy level of the C₆₀ EEL and further collected by the Al cathode. Therefore, a photo-induced charge transfer is expected to occur within the Cs_{0.15}FA_{0.85}PbI₃.PDDTT BHJ composite thin film, which would result in enlarged JSC.

The current density versus voltage (J-V) characteristics of the PSCs are shown in Fig. 3c and Fig. S2. The device performance parameters of PSCs are summarized in Table 1 and Table S1. Under the reverse scan direction and the scan rate of 0.6 V/s, the PSCs based on pristine $Cs_{0.15}FA_{0.85}PbI_3$ thin film exhibit a J_{SC} of 23.32 (22.87 \pm 0.65) mA/cm²,

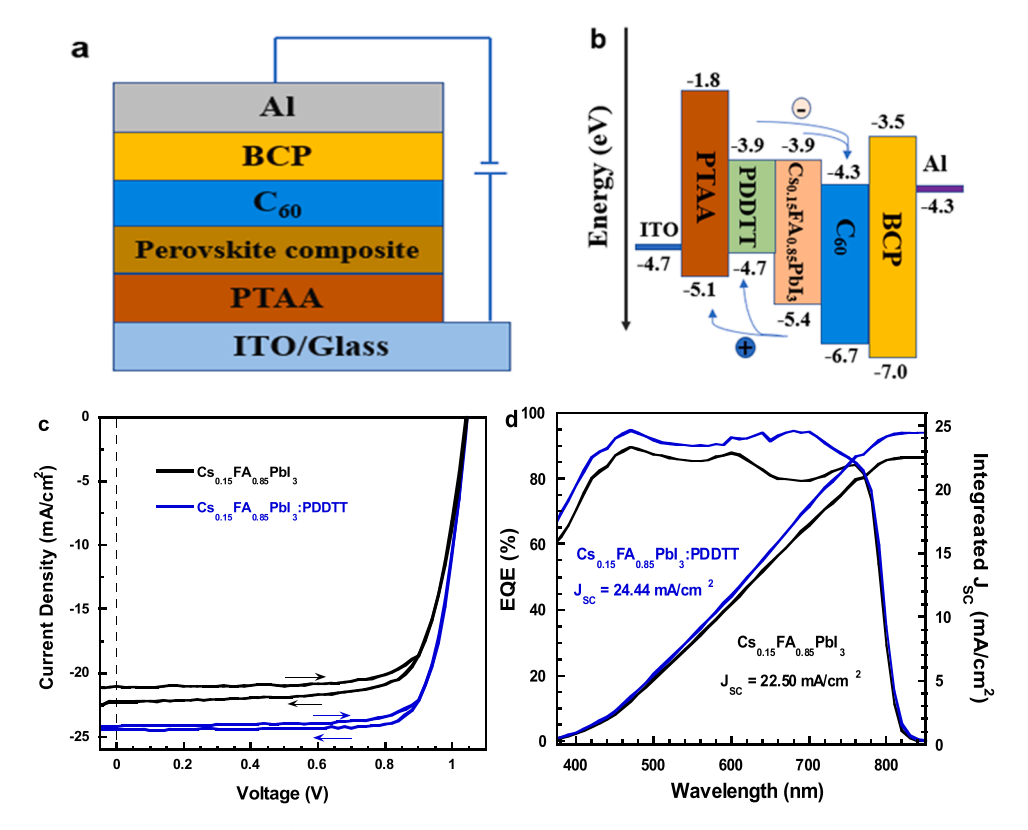


Fig. 3. a) Device architecture of PSCs, **b)** the LUMO and HOMO energy levels of PTTA, PDDTT, Cs_{0.15}FA_{0.85}PbI₃, C₆₀, and BCP, and the work functions of the ITO and Al electrodes, **c)** the J-V characteristics of and **d)** the EQE of the PSCs based on either pristine Cs_{0.15}FA_{0.85}PbI₃ thin film or the Cs_{0.15}FA_{0.85}PbI₃:PDDTT BHJ composite thin film.

Table 1Device performance of PSCs under different scan directions.

Photoactive layer	V _{OC} (V)	J_{SC} (mA/cm ²)	FF (%)	PCE (%)	HI
Cs _{0.15} FA _{0.85} PbI ₃ (forward)	$1.04~(1.03\pm0.01)$	$22.21 \; (21.88 \pm 0.70)$	77 (74 \pm 4)	$17.50~(17.10\pm0.40)$	0.030
Cs _{0.15} FA _{0.85} PbI ₃ (reverse)	$1.04~(1.03\pm0.01)$	$23.31~(22.87\pm0.65)$	$75~(73\pm 3)$	$18.03~(17.54\pm0.49)$	
Cs _{0.15} FA _{0.85} PbI ₃ :PDDTT (forward)	$1.04~(1.03\pm0.01)$	$25.34\ (24.97\pm0.51)$	$79~(77\pm4)$	$20.83\ (20.44\pm0.52)$	0.012
Cs _{0.15} FA _{0.85} PbI ₃ :PDDTT (reverse)	$1.04~(1.03\pm0.01)$	$25.51\ (25.30\pm0.43)$	$80~(78\pm4)$	$21.08\ (20.51\pm0.57)$	

an open-circuit voltage (V_{OC}) of 1.04 (1.03 \pm 0.01) V and a fill factor (FF) of 75% (73 \pm 3%), with a corresponding PCE of 18.03% (17.54 \pm 0.49%). Whereas under the forward scan direction and the scan rate of 0.6 V/s, the PSCs based on pristine $Cs_{0.15}FA_{0.85}PbI_3$ thin film exhibit a J_{SC} of 22.21 (21.88 \pm 0.70) mA/cm², a V_{OC} of 1.04 (1.03 ± 0.01) V and a FF of 77% (74 \pm 4%), with a corresponding PCE of 17.50% (17.10 \pm 0.40%). These device performance parameters are consistent with reported values [30]. The PSCs based on the Cs_{0.15}FA_{0.85}PbI₃:PDDTT BHJ composite thin film incorporated with 0.02 mg/mL of PDDTT exhibit the best device performance. Under the reverse scan direction and the scan rate of 0.6 V/s, the PSCs based on the Cs_{0.15}FA_{0.85}PbI₃:PDDTT BHJ composite thin film exhibit a J_{SC} of 25.51 $(25.30 \pm 0.43) \text{ mA/cm}^2$, a V_{OC} of 1.04 $(1.03 \pm 0.01) \text{ V}$ and a FF of 80% $(78 \pm 4\%)$, with a corresponding PCE of 21.08% $(20.51 \pm 0.57\%)$, whereas under the forward scan direction and the scan rate of 0.6 V/s, the PSCs based on the Cs_{0.15}FA_{0.85}PbI₃:PDDTT BHJ composite thin film exhibit a J_{SC} of 25.34 (24.97 \pm 0.51) mA/cm², a V_{OC} of 1.04 (1.03 ± 0.01) V and a FF of 79% (77 \pm 4%), with a corresponding PCE of 20.83% (20.44 \pm 0.52%). The PSCs based on the $Cs_{0.15}FA_{0.85}PbI_3$: PDDTT BHJ composite thin film have more than 16% enhancement in PCEs compared to those based on pristine Cs_{0.15}FA_{0.85}PbI₃ thin film.

As described above, both PSCs exhibit different PCEs under different scan directions, which indicates that both PSCs possess different photocurrent hysteresis [35–39]. The photocurrent hysteresis is defined

as photocurrent hysteresis index (HI), which is defined as HI = (PCE_{T-everse} – PCE_{forward})/PCE_{reverse} [40]. At the scan rate of 0.6 V/s, the HI of 0.03 is calculated for the PSCs based on pristine $Cs_{0.15}FA_{0.85}PbI_3$ thin film, whereas the HI of 0.012 is calculated for the PSCs based on the $Cs_{0.15}FA_{0.85}PbI_3$:PDDTT BHJ composite thin film. Such a small HI value demonstrates that the PSCs based on the $Cs_{0.15}FA_{0.85}PbI_3$:PDDTT BHJ composite thin film possess suppressed photocurrent hysteresis [41].

Fig. 3d presents the external quantum efficiency (EQE) of PSCs and the integrated J_{SC} based on the EQE spectra of PSCs. Compared to the PSCs based on pristine $Cs_{0.15}FA_{0.85}PbI_3$ thin film, enhanced EQE values are observed from the PSCs based on the $Cs_{0.15}FA_{0.85}PbI_3$:PDDTT BHJ composite thin film, which indicates that PDDTT indeed contributes J_{SC} . The integrated J_{SC} values are 22.50 mA/cm² and 24.44 mA/cm² for the PSCs based on pristine $Cs_{0.15}FA_{0.85}PbI_3$ thin film and the PSCs based on the $Cs_{0.15}FA_{0.85}PbI_3$:PDDTT BHJ composite thin film, respectively. These integrated J_{SC} values are in good agreement with those extracted from the J-V characteristics (Fig. 3c).

To understand the underlying physics of enhanced J_{SC} , scan electron microscopy (SEM) is carried out to investigate the film morphology of perovskite photoactive layers. Fig. 4a, b presents the SEM images of pristine $Cs_{0.15}FA_{0.85}PbI_3:PDDTT\ BHJ$ composite thin film. The grain size of pristine $Cs_{0.15}FA_{0.85}PbI_3:PDDTT\ BHJ$ composite the grain size of the ~ 100 nm, whereas the grain size of the $Cs_{0.15}FA_{0.85}PbI_3:PDDTT\ BHJ$ composite thin film incorporated with

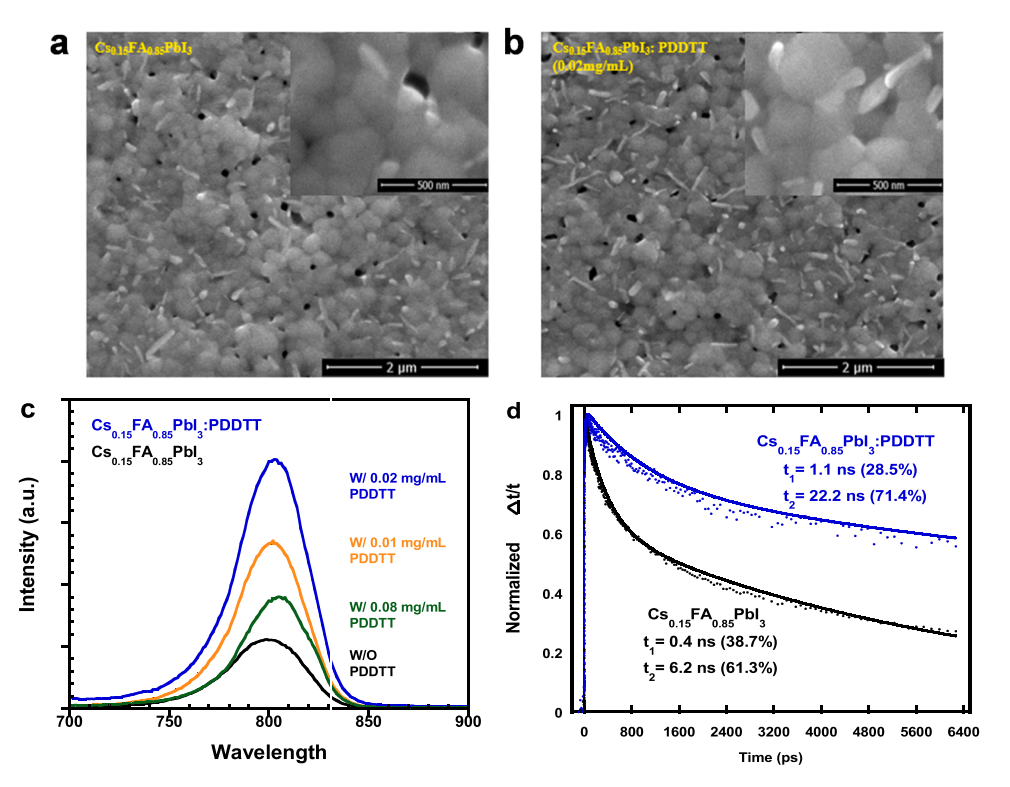


Fig. 4. The top-view SEM image of a) pristine $Cs_{0.15}FA_{0.85}PbI_3$ thin film and b) the $Cs_{0.15}FA_{0.85}PbI_3$:PDDTT BHJ composite thin film, c) the steady-state photoluminescence (PL) spectra of pristine $Cs_{0.15}FA_{0.85}PbI_3$ and the $Cs_{0.15}FA_{0.85}PbI_3$:PDDTT BHJ composite thin films, d) the transient absorption spectra of pristine $Cs_{0.15}FA_{0.85}PbI_3$:thin film and the $Cs_{0.15}FA_{0.85}PbI_3$:PDDTT BHJ composite thin film.

0.02~mg/mL of PDDTT is estimated to be $\sim300~nm$. Moreover, the grain size of the $Cs_{0.15}FA_{0.85}PbI_3:PDDTT$ BHJ composite thin film incorporated with 0.08~mg/mL of PDDTT is estimated to be $\sim250~nm$ (Fig. S3). Large grain sizes imply that the $Cs_{0.15}FA_{0.85}PbI_3:PDDTT$ BHJ composite thin films possess enhanced charge carrier mobilities, which is in good agreement with the observation described above. As a result, the PSCs based on the $Cs_{0.15}FA_{0.85}PbI_3:PDDTT$ BHJ composite thin film exhibit boosted J_{SC} .

Fig. 4c presents the steady-state photoluminescence (PL) spectra of pristine $Cs_{0.15}FA_{0.85}PbI_3$; thin film and the $Cs_{0.15}FA_{0.85}PbI_3$; PDDTT BHJ composite thin films. It is found that the PL intensities of the $Cs_{0.15}FA_{0.85}PbI_3$; PDDTT BHJ composite thin films are increased and then decreased along with increased concentrations of PDDTT. Such tuned PL intensities are probably ascribed to the smooth and rough surfaces of perovskite thin films induced by PDDTT (Figs. 4a, b and S3). Moreover, compared to pristine $Cs_{0.15}FA_{0.85}PbI_3$ thin film, the $Cs_{0.15}FA_{0.85}PbI_3$; PDDTT BHJ composite thin films exhibit enhanced PL intensities, which indicates that the non-radiation recombination within the $Cs_{0.15}FA_{0.85}PbI_3$; PDDTT BHJ composite thin film is suppressed. Such enhanced PL is ascribed to the enlarged grain sizes of $Cs_{0.15}FA_{0.85}PbI_3$ induced by PDDTT. The suppressed non-radiation recombination could boost photocurrent of the PSCs by the $Cs_{0.15}FA_{0.85}PbI_3$; PDDTT BHJ composite thin film.

Fig. 4d displays the transient absorption dynamics of thin film. Pristine $Cs_{0.15}FA_{0.85}PbI_3$ thin film has a decay lifetime of 6.2 nanoseconds (ns), while the $Cs_{0.15}FA_{0.85}PbI_3$:PDDTT BHJ composite thin film has a decay lifetime of 22.2 ns. The longer lifetime observed from the $Cs_{0.15}FA_{0.85}PbI_3$:PDDTT BHJ composite thin film indicates that the $Cs_{0.15}FA_{0.85}PbI_3$:PDDTT BHJ composite thin film possesses superior film quality, larger crystallinity, larger grain size, and reduced trap densities compared to $Cs_{0.15}FA_{0.85}PbI_3$: thin film. On the other hand, the long decay lifetime demonstrates that the $Cs_{0.15}FA_{0.85}PbI_3$:PDDTT BHJ composite thin film probably possesses longer-lived charge carriers compared to pristine $Cs_{0.15}FA_{0.85}PbI_3$ thin film [42], which implies that

a photo-induced charge transfer probably takes place within the $Cs_{0.15}FA_{0.85}PbI_3:PDDTT$ BHJ composite thin film. These observations further verify the hypothesis described above (Fig. 3b). The pseudocolor transient absorption spectra (Fig. S4) further confirm that a photo-induced charge transfer probably takes place within the $Cs_{0.15}FA_{0.85}PbI_3:PDDTT$ BHJ composite thin film. Therefore, as expected, the PSCs based on the $Cs_{0.15}FA_{0.85}PbI_3:PDDTT$ BHJ composite thin film exhibit boosted J_{SC} and PCE.

The transient photocurrent (TPC) measurement is conducted to investigate the charge generation and transport kinetics in PSCs [43,44]. Fig. 5a presents the normalized TPC curves of PSCs. Under the short-circuit condition, all PSCs possess a similar transient photocurrent curve. In the beginning, the TPC curves are tended to be linear since all charge carriers are extracted during a short time [44,45]. However, a significant difference in the TPC curves is observed from these two types of PSCs after ~ 50 ns. Such differences are originated from the trap and de-trap processes of charge carriers [43]. Through extrapolating the linear region to zero, the lifetime of charge extraction is estimated [44]. The PSCs based on pristine Cs_{0.15}FA_{0.85}PbI₃ thin film possess a lifetime of ~ 140 ns, whereas the PSCs based on the Cs_{0.15}FA_{0.85}PbI₃:PDDTT BHJ composite thin film has a lifetime of ~ 120 ns. The short lifetime indicates a fast sweep-out process of the charge carrier [46]. Thus, the PSCs based on the Cs_{0.15}FA_{0.85}PbI₃:PDDTT BHJ composite thin film exhibit enlarged J_{SC}, consequently, boosted PCE, with respect to those based on pristine Cs_{0.15}FA_{0.85}PbI₃ thin film. Moreover, increased photocurrent densities are observed from the PSCs based on the Cs_{0.15}FA_{0.85}PbI₃:PDDTT BHJ composite thin film (Fig. S5b) further indicating that the charge recombination within the PSCs based on the Cs_{0.15}FA_{0.85}PbI₃:PDDTT BHJ composite thin film is suppressed, as compared to those based on pristine Cs_{0.15}FA_{0.85}PbI₃ thin film. As a result, the PSCs based on the Cs_{0.15}FA_{0.85}PbI₃:PDDTT BHJ composite thin film exhibit enlarged J_{SC}, consequently, boosted PCE.

The light intensity-dependent J_{SC} and V_{OC} are further investigated to understand the underlying physics of enhanced J_{SC} [47–49], and the

L. Shen et al. Nano Energy 93 (2022) 106907

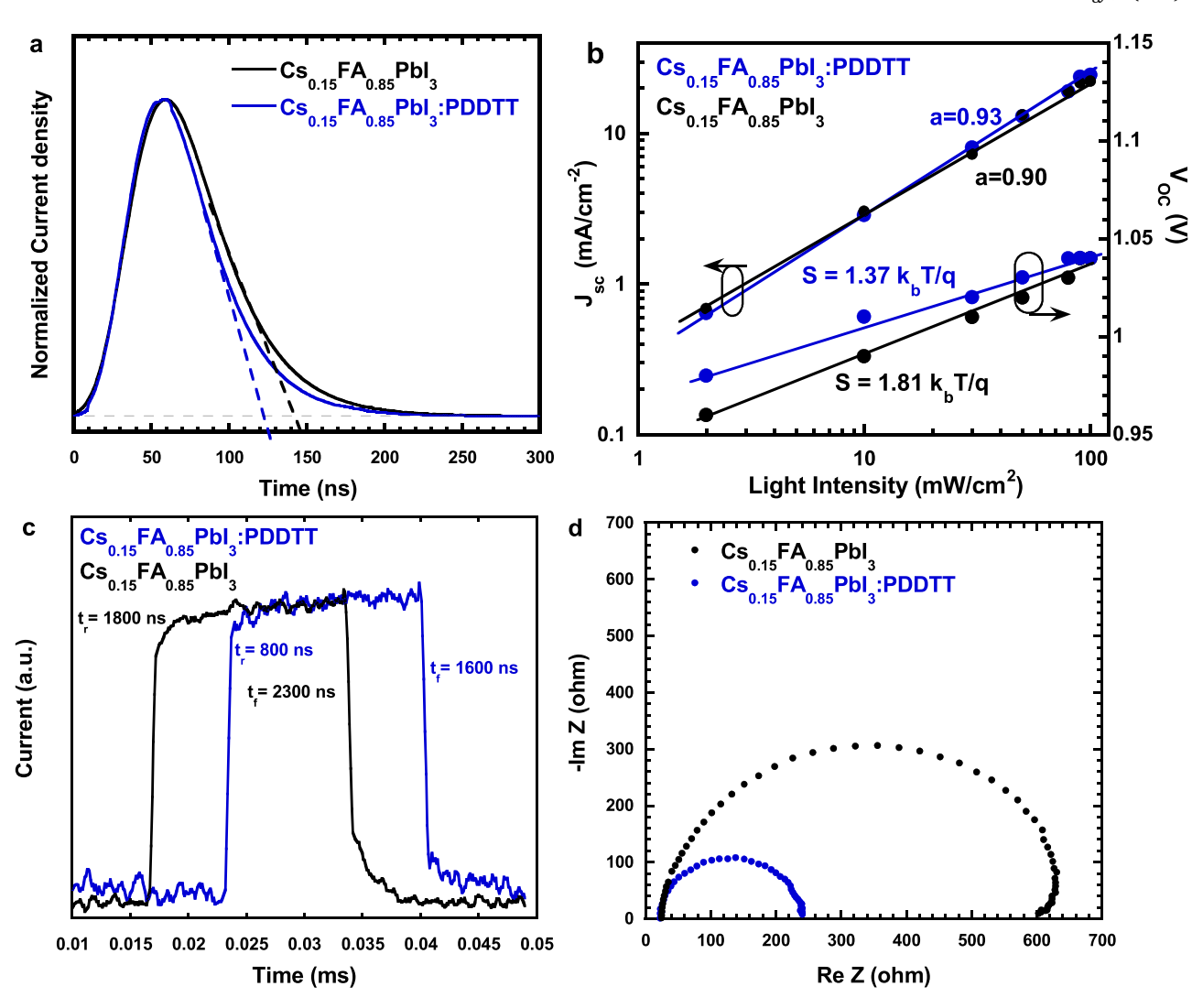


Fig. 5. a) Normalized transient photocurrent curves of PSCs, b) the light intensity dependent J_{SC} and V_{OC} of PSCs, c) the transient photocurrent measured with an optical chopper controlled at $\lambda = 532$ nm laser pulse and d) the J-V characteristics of PSCs measured in dark, where the PSCs are based on either pristine $Cs_{0.15}FA_{0.85}PbI_3$ thin film or the $Cs_{0.15}FA_{0.85}PbI_3$:PDDTT BHJ composite thin film.

results are shown in Fig. 5b. Under the open-circuit condition, $V_{\rm OC}$ has been described as $V_{\rm OC}=n(K_bT/q)ln(I)$ (where K_b is the Boltzmann constant, T is the temperature in Kelvin and q is the elementary charge, and n is a constant). As n equals 1, the bimolecular recombination is dominated in solar cells, whereas as n equals 2, the monomolecular recombination is dominated in solar cells [50,51]. The slopes of 1.81 K_bT/q and 1.37 K_bT/q are observed from the PSCs based on either pristine $Cs_{0.15}FA_{0.85}PbI_3$; thin film or the $Cs_{0.15}FA_{0.85}PbI_3$; PDDTT BHJ composite thin film. Thus, compared to the PSCs based on pristine $Cs_{0.15}FA_{0.85}PbI_3$; thin film, a weak monomolecular charge recombination process takes place within the PSCs based on the $Cs_{0.15}FA_{0.85}PbI_3$; PDDTT BHJ composite thin film, resulting in enhanced J_{SC} and PCEs.

Moreover, J_{SC} related to the light intensity is described as $J_{SC} \in I^a$ (where I is the light intensity and a is the scaling exponent) [52]. A large a indicates a weak charge carrier recombination happens in solar cells [53,54]. All PSCs possess a power-law dependence of J_{SC} on the light intensity. The PSCs based on the $C_{50.15}FA_{0.85}PbI_3$:PDDTT BHJ composite thin film exhibit a of 0.93, which is larger than that (0.90) observed from the PSCs based on pristine $C_{50.15}FA_{0.85}PbI_3$ thin film. Thus, the PSCs by the $C_{50.15}FA_{0.85}PbI_3$:PDDTT BHJ composite thin film exhibit larger J_{SC} than that based on pristine $C_{50.15}FA_{0.85}PbI_3$ thin film.

In addition, the trap density (N_t) , which is described as $N_t = (2\epsilon_0 \epsilon V_{TFL})/(eL^2)$ (where V_{TFL} is the trap-filled limit voltage, L is the

thickness of the active layer, ε_0 is the vacuum permittivity (8.85 imes 10^{-12} C V⁻¹ m⁻¹), ε is the relative dielectric constant of the active layer, and eis the elementary electric charge, respectively) [32], is further investigated. It is found that the Cs_{0.15}FA_{0.85}PbI_{3:}PDDTT BHJ composite thin film possesses different V_{TFL} values compared to pristine $Cs_{0.15}FA_{0.85}PbI_3$ thin film. For the electron transport, the V_{TFL} values are reduced to 0.12 V for the Cs_{0.15}FA_{0.85}PbI_{3:}PDDTT BHJ composite thin film from 0.27~V for pristine $Cs_{0.15}FA_{0.85}PbI_3$ thin film. For the hole transport, the V_{TFL} values are dropped to 0.56 V for the Cs_{0.15}FA_{0.85}PbI_{3:}PDDTT BHJ composite thin film from 0.78 V for pristine Cs_{0.15}FA_{0.85}PbI₃ thin film. Thus, the estimated hole-trap and electron-trap densities for the Cs_{0.15}FA_{0.85}PbI₃:PDDTT BHJ composite thin film are $1.08 \times 10^{16} \text{ cm}^{-3}$ and $2.32 \times 10^{15} \text{ cm}^{-3}$, respectively. Whereas the estimated hole-trap and electron-trap densities for pristine $Cs_{0.15}FA_{0.85}PbI_3$ thin film are 5.15×10^{16} cm⁻³ and 6.91×10^{15} cm⁻³, respectively. Both the hole-trap and electron-trap densities of the Cs_{0.15}FA_{0.85}PbI₃·PDDTT BHJ composite thin film are smaller than those for pristine CsPbI2Br thin film. Such reduced charge-trap densities are ascribed to the reduced point-defect at the atomic scale and the large crystal grain size (Fig. 4a and b). Thus, as expected, the PSCs based on the Cs_{0.15}FA_{0.85}PbI_{3:}PDDTT BHJ composite thin film exhibit enhanced

The temporal photocurrent response is carried out to understand

L. Shen et al. Nano Energy 93 (2022) 106907

suppressed photocurrent hysteresis of PSCs. Note that the response time is significantly related to the charge transport and collection [55]. The rise and fall times are defined as the time interval required for the photoresponse to rise/decay from 10/90% to 90/10% of its peak photocurrent value, respectively [56]. The transient photocurrent measured with an optical chopper (a frequency of 2 kHz) controlled by λ of 532 nm laser pulse is shown in Fig. 5c. A rise time of 1.8 µs and a fall time of 2.3 µs are observed from the PSCs based on pristine $Cs_{0.15}FA_{0.85}PbI_3$ thin film; whereas a rise time of 0.8 μs and a fall time of 1.6 μs are observed from the PSCs based on the Cs_{0.15}FA_{0.85}PbI₃:PDDTT BHJ composite thin film. A fast response time observed from the PSCs based on the Cs_{0.15}FA_{0.85}PbI₃:PDDTT BHJ composite thin film indicates there is less hysteretic current when the photon excites, resulting in suppressed photocurrent hysteresis [35,56,57]. Furthermore, suppressed counter ions (Pb²⁺ and I') (Figs. 2d, 1D GIWAXS profiles) indicate that the PSCs based on the Cs_{0.15}FA_{0.85}PbI₃:PDDTT BHJ composite thin film possess reduced photocurrent hysteresis [34].

The impedance spectroscopy (IS) of PSCs is carried out to investigate the detailed electrical properties of PSCs. Fig. 5d presents the Nyquist plot of PSCs measured in dark. The charge-transfer resistance ($R_{\rm CT}$) values for the PSCs based on either pristine $Cs_{0.15}FA_{0.85}PbI_3$ thin film or

the $Cs_{0.15}FA_{0.85}PbI_3$:PDDTT BHJ composite thin film are calculated to be 600 Ω and 240 Ω , respectively. The smaller R_{CT} is originated from a high-quality thin film and suppressed charge carrier recombination within the $Cs_{0.15}FA_{0.85}PbI_3$:PDDTT BHJ composite thin film. Thus, the PSCs based on the $Cs_{0.15}FA_{0.85}PbI_3$:PDDTT BHJ composite thin film possess higher FF compared to those based on pristine $Cs_{0.15}FA_{0.85}PbI_3$ thin film.

To explore the same V_{OC} observed from the PSCs based on either pristine $Cs_{0.15}FA_{0.85}PbI_3$; thin film or the $Cs_{0.15}FA_{0.85}PbI_3$; PDDTT BHJ composite thin film, the J-V characteristics of PSCs measured in dark are conducted and the results are shown in Fig. 6a. Under the reverse biases, the dark current densities of both PSCs are nearly the same. According to the electronic diodes model [58,59], V_{OC} is described as $V_{OC} \approx (nkT/q) \ln(J_{SC}/J_0)$ (where J_0 is the reverse dark current density, q is the electron charge, n is the diode ideality factor, k is Boltzmann's constant, and T is the temperature). A similar value of J_0 observed from two different PSCs indicates that a similar value of V_{OC} for both PSCs. Thus, both PSCs exhibit a similar V_{OC} .

To estimate the built-in potential (V_{bi}) and the interfacial charge density (N) of PSCs, the capacitor versus voltage (C-V) characteristics of PSCs are conducted. According to the Mott-Schottky law of $C^{-2}=\frac{2(V_{bi}-V)}{q\varepsilon\varepsilon_0A^2\eta_c}$

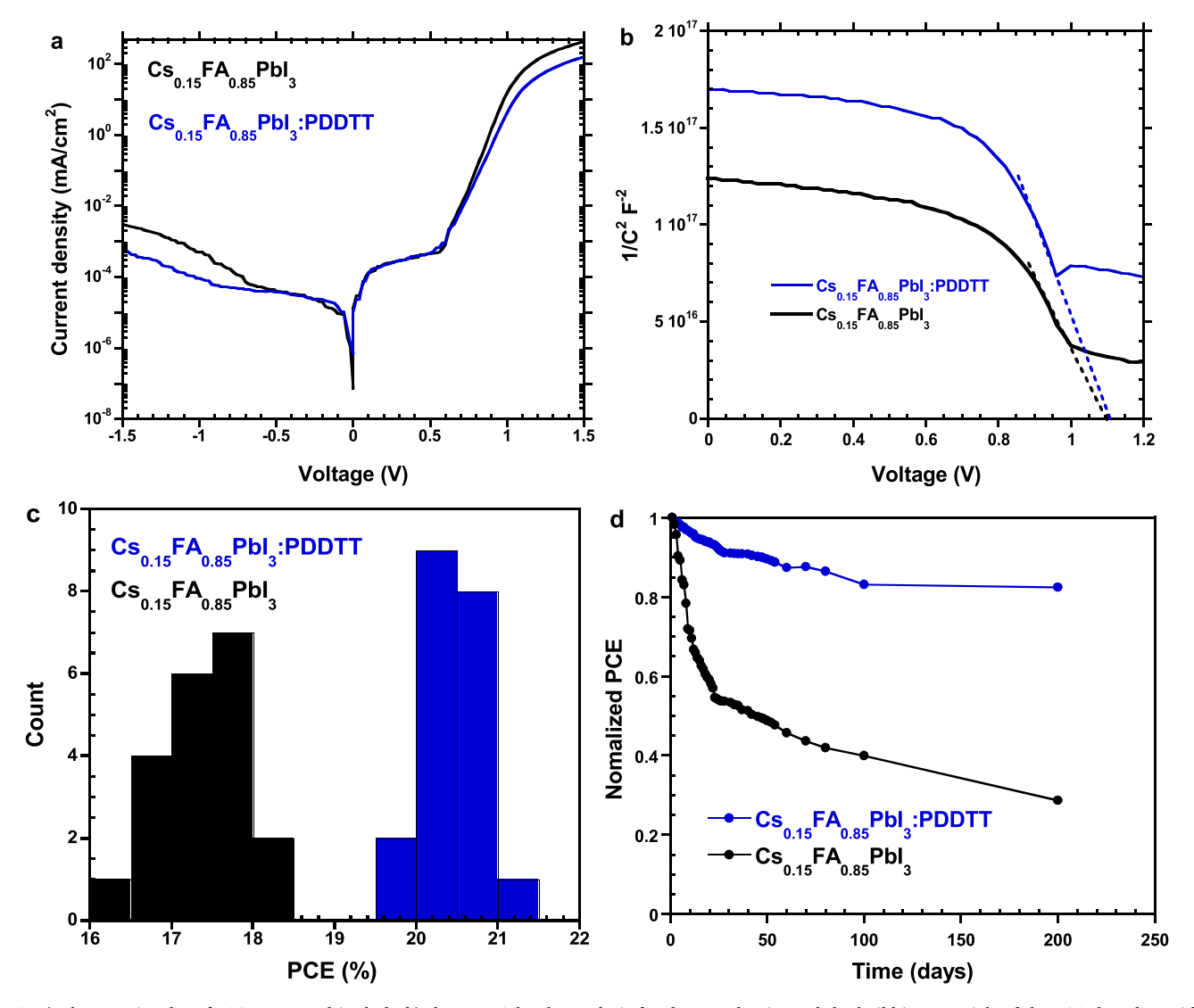


Fig. 6. a) The Nyquist plot of PSCs measured in dark, b) the Mott-Schottky analysis for the trap-density and the build-in potentials of the PSCs based on either pristine $Cs_{0.15}FA_{0.85}PbI_3$; or the $Cs_{0.15}FA_{0.85}PbI_3$; PDDTT BHJ composite thin film, c) the histogram of PSCs, where PSCs are based on either pristine $Cs_{0.15}FA_{0.85}PbI_3$; PDDTT BHJ composite thin film, and d) the shelf stability of un-encapsulated PSCs measured in the glovebox with a nitrogen atmosphere at room temperature, where PSCs are based on either pristine $Cs_{0.15}FA_{0.85}PbI_3$; thin film or the $Cs_{0.15}FA_{0.85}PbI_3$; PDDTT BHJ composite thin film.

(where V is applied bias, q is the elementary charge, ε is the dielectric constant of perovskites, ε_0 is the vacuum permittivity, n_c is the charge carrier density, and A is the active area, respectively), the V_{hi} is the intercept on the bias of the linear fitting line, and the *N* is obtained from the slope of the linear fitting [25,60]. Fig. 6b presents the C^{-2} -V plot of PSCs. The PSCs based on pristine Cs_{0.15}FA_{0.85}PbI₃ thin film exhibit a V_{bi} of 1.10 V, which is the same as that based on the Cs_{0.15}FA_{0.85}PbI₃: PDDTT BHJ composite thin film. These results indicate that the PSCs based on pristine $Cs_{0.15}FA_{0.85}PbI_3$ thin film exhibit the same V_{OC} as those based on the Cs_{0.15}FA_{0.85}PbI₃:PDDTT BHJ composite thin film. Moreover, the slope of the C⁻²-V line for the PSCs based on pristine $Cs_{0.15}FA_{0.85}PbI_3$ thin film is estimated to be -3.64×10^{17} , while the slope for the PSCs based on the $Cs_{0.15}FA_{0.85}PbI_3$:PDDTT BHJ composite thin film is -5.24×10^{17} . Such a large absolute slope value of the PSCs based on the $Cs_{0.15}FA_{0.85}PbI_3$:PDDTT BHJ composite thin film indicates that this type of PSCs possesses a smaller interfacial charge density [32, 61]. As a result, the surface charge carrier recombination is suppressed, resulting in enhanced J_{SC} for the PSCs based on the Cs_{0.15}FA_{0.85}PbI₃: PDDTT BHJ composite thin film.

The reproducibility of PSCs is further studied. The statistical histograms of the photovoltaic parameters for both PSCs from counted numbers of 20 devices are shown in Fig. 6c. The PSCs based on pristine $Cs_{0.15}FA_{0.85}PbI_3$; thin films exhibit a severe deviation in PCEs, compared to the PSCs based on the $Cs_{0.15}FA_{0.85}PbI_3$:PDDTT BHJ composite thin film. Thus, the reproducibility of the PSCs based on the $Cs_{0.15}FA_{0.85}PbI_3$: PDDTT BHJ composite thin film is significantly higher than those based on pristine $Cs_{0.15}FA_{0.85}PbI_3$; thin film. Such high reproducibility is ascribed to superior film quality and enlarged crystal sizes of the $Cs_{0.15}FA_{0.85}PbI_3$:PDDTT BHJ composite thin film induced by PDDTT.

Fig. 6d presents the self-stability of unencapsulated PSCs stored in the glove box with nitrogen atmosphere at room temperature. After 200 days, the PSCs based on pristine $Cs_{0.15}FA_{0.85}PbI_3$ thin film decay 70% of their initial PCE value, whereas the PSCs based on the $Cs_{0.15}FA_{0.85}PbI_3$: PDDTT BHJ composite thin film only drops less than 20% of their initial PCE value at the same period. Such boosted stability is originated from superior film quality and enlarged crystal sizes of the $Cs_{0.15}FA_{0.85}PbI_3$: PDDTT BHJ composite thin film induced by PDDTT.

3. Conclusion

In conclusion, we reported high-performance bulk heterojunction (BHJ) perovskite solar cells (PSCs) based on n-type Cs_{0.15}FA_{0.85}PbI₃ perovskite incorporated with p-type low optical gap conjugated polymer, PDDTT. Compared to pristine Cs_{0.15}FA_{0.85}PbI₃ thin film, it was found that the Cs_{0.15}FA_{0.85}PbI₃:PDDTT BHJ composite thin film possessed enhanced and balanced charge carrier mobilities, enlarged crystal sizes, and suppressed non-radiation charge carrier recombination. Moreover, a photo-induced charge transfer took place within the Cs_{0.15}FA_{0.85}PbI₃:PDDTT BHJ composite thin film. As a result, the PSCs based on the Cs_{0.15}FA_{0.85}PbI₃:PDDTT BHJ composite thin film exhibited enhanced power conversion efficiency (PCE) of 21.08%. In addition, unencapsulated BHJ PSCs possess remarkably enhanced stability (as they retain 80% of their initial PCE after ~ 200 days in ambient conditions) and diminished photocurrent hysteresis (photocurrent hysteresis index of 0.012) compared to those based on pristine Cs_{0.15}FA_{0.85}PbI₃ thin film. All these results demonstrated that the PSCs with a BHJ device structure is one of the facile ways to approach high-performance PSCs.

4. Materials and methods

4.1. Materials

Poly-[bis(4-phenyl)(2,4,6-trimethylphenyl)amine] (PTAA), molybdenum(VI) oxide (99.97%), ethyl alcohol (≥ 99.5%), toluene (anhydrous, 99.8%), dimethyl sulfoxide (DMSO, anhydrous, 99.9%), N, N-dimethylformamide (DMF, anhydrous, 99.8%), bathocuproine (BCP,

99.99%), and aluminum (Al) and silver (Ag) slugs were purchased from Sigma-Aldrich. Lead iodide (PbI₂, 99.9985% metals basis), cesium iodide (99.9985%), and Tin(IV) oxide (15% in H₂O colloidal dispersion) were purchased from Alfa Aesar. C_{60} (99.95% carbon powder) was purchased from Pure60oliveoil. Formamidinium iodide (FAI) was purchased from Greatcell Solar. All chemicals were used as received without further purification. Poly(5,7-bis(4-decanyl-2-thienyl)-thieno (3,4-b)diathiazole-thiophene-2,5) (PDDTT) was synthesized by us and reported previously [26].

4.2. Preparation of perovskite thin films

Pristine $Cs_{0.15}FA_{0.85}PbI_3$ precursor solution was prepared by adding PbI_2 (461.0 mg, 1 mmol), FAI (146.2 mg, 0.85 mmol) and CsI (39.0 mg, 0.15 mmol) into a solution of DMF and DMSO (1 mL 4:1 v/v%). The $Cs_{0.15}FA_{0.85}PbI_3$:PDDTT precursor solution was prepared by mixing $Cs_{0.15}FA_{0.85}PbI_3$ precursor solution with different concentrations of PDDTT in 1 mL DMF:DMF (4:1 v/v%). Perovskite layer was spin-coated on the substrates by a spin-cast method with a spin speed of 1500 RPM for 10 s (s) and then 5000 RPM for 40 s. After that, the anti-solvent ethyl alcohol was dropped onto the as-cast perovskite thin films and left for at least 10 s and continuously completed spin-casting procedure Then perovskite thin films were thermally annealed at 100 °C for 1 h.

4.3. Characterization of perovskite thin films

UV-vis absorption spectra of thin films were recorded on an HP 8453 spectrophotometer. Photoluminescence (PL) spectra of thin films were recorded on a HORIBA Fluorolog-3 fluorescence spectrophotometer. The transient absorption spectra were obtained by a femtosecond laser (Coherent) at 5KHz and commercial transient absorption spectroscopy (Ultrafast Systems). The pump pulse 400 nm at $10\,\mu W$ was generated with an optical parametric amplifier (OPA) and the probe white light pulse was created by focusing a small portion of 800 nm pulse onto a sapphire. The samples were stored in the nitrogen-filled glovebox and tested right after exposure to air. It was found that both thin films show the ground-state bleaching (GSB) around 770 nm, due to the photoexcited electrons in the excited state and holes in the ground state that can reduce the absorption of probed photons for the corresponding transition (Pauli exclusion principle) [35,42]. The carrier dynamics were fitted with the software Igor. The time-resolved photocurrent was recorded with a 300 MHz Tektronix DPO3034 oscilloscope by measuring the voltage drop across a 5 Ω RF sensor resistor in series with the device. 5 Ω was chosen to further minimize the RC time constant of the setup. The grazing-incidence wide-angle x-ray scattering (GIWAXS) was performed on the high-resolution GIWAXS beamline (Sector 8-ID-E) in the Advanced Photon Source, Argonne National Laboratory [62]. The top view SEM images were obtained by using a field emission scanning electron microscope (JEOL-7401), where the samples were prepared from the semi-finished solar cells. The film thicknesses were measured by Dektak 150 surface profilometer with a scan rate of 0.06 mm/s. The XRD patterns were obtained by a Rigaku Smartlab.

4.4. Fabrication of PSCs

The pre-cleaned ITO/glass substrates were firstly treated in a UV-ozone cleaner for 40 min. Then ITO/glass substrates were transferred into a glove box with a nitrogen atmosphere. A ~ 8 nm PTAA layer was deposited onto the top of ITO/glass substrates by spin-coating from 2 mg/mL PTAA toluene solution at 6000 RPM for 40 s, followed by thermal annealing at 100 °C for 10 min (min). After the PTAA layer was cooled down to room temperature naturally, either $Cs_{0.15}FA_{0.85}PbI_3$ thin film or the $Cs_{0.15}FA_{0.85}PbI_3$:PDDTT BHJ composite thin film was deposited on the top of the PTAA layer by spin-coated method from the corresponding solutions as described above. The film thickness of both $Cs_{0.15}FA_{0.85}PbI_3$ and $Cs_{0.15}FA_{0.85}PbI_3$:PDDTT thin films were measured

to be 480 nm. Afterward, a ~ 15 nm C_{60} thin layer, a ~ 8 nm BCP thin layer, and ~ 100 nm Al were consequently thermally deposited in a vacuum with a base pressure of 4 \times 10^{-6} mbar. The effective device area was measured to be 0.043 cm².

4.5. Characterization of PSCs

The current density versus voltage (J-V) characteristics of PSCs under white light illumination was obtained by using a Keithley 2400 source meter. The white light was generated by an AM 1.5 G solar simulator (Newport, 91160-1000) and white light intensity was calibrated by a mono-silicon detector (with KG-5 visible color filter) from the National Renewable Energy Laboratory. The external quantum efficiency (EQE) measurement was obtained by using the solar cell quantum efficiency measurement system (QEX10) from PV measurements with a 300 W steady-state xenon lamp as the source light. The impedance spectrum (IS) was obtained using an HP 4194 A impedance/ gain-phase analyzer under dark conditions, with an oscillating voltage of 10 mV from 5 Hz to 105 Hz. PSCs were held at the voltage closing to the corresponding open-circuit voltage (Voc), while the IS was carried out. The capacitance-voltage (C-V) testing was also performed on the same setup. Transient photocurrent (TPC) measurement was taken with a custom-built, fully automated setup [63]. The whole process of TPC is reported previously [25,45,51,63].

Declaration of Competing Interest

The authors declare that they have no known competing financial interests or personal relationships that could have appeared to influence the work reported in this paper.

Acknowledgments

The authors at the University of Akron acknowledge the National Science Foundation, USA (ECCS/EPMD1903303) for financial support.

Appendix A. Supporting information

Supplementary data associated with this article can be found in the online version at doi:10.1016/j.nanoen.2021.106907.

References

- [1] A. Kojima, K. Teshima, Y. Shirai, T. Miyasaka, Organometal halide perovskites as visible-light sensitizers for photovoltaic cells, J. Am. Chem. Soc. 131 (2009) 6050–6051, https://doi.org/10.1021/ja809598r.
- [2] M. Gratzel, The rise of highly efficient and stable perovskite solar cells, Acc. Chem. Res. 50 (2017) 487–491, https://doi.org/10.1021/acs.accounts.6b00492.
- [3] N.J. Jeon, H. Na, E.H. Jung, T.-Y. Yang, Y.G. Lee, G. Kim, H.-W. Shin, S.I. Seok, J. Lee, J. Seo, A fluorene-terminated hole-transporting material for highly efficient and stable perovskite solar cells, Nat. Energy 3 (2018) 682–689, https://doi.org/10.1038/s41560-018-0200-6.
- [4] J. Seo, J.H. Noh, S.I. Seok, Rational strategies for efficient perovskite solar cells, Acc. Chem. Res. 49 (2016) 562–572, https://doi.org/10.1021/acs. accounts 5b00444
- [5] N.J. Jeon, J.H. Noh, W.S. Yang, Y.C. Kim, S. Ryu, J. Seo, S.I. Seok, Compositional engineering of perovskite materials for high-performance solar cells, Nature 517 (2015) 476–480. https://doi.org/10.1038/nature14133.
- [6] W. Xu, L. Zheng, X. Zhang, Y. Cao, T. Meng, D. Wu, L. Liu, W. Hu, X. Gong, Efficient perovskite solar cells fabricated by Co partially substituted hybrid perovskite, Adv. Energy Mater. 8 (2018), 1703178, https://doi.org/10.1002/aenm.201703178.
- [7] L. Chu, W. Ahmad, W. Liu, J. Yang, R. Zhang, Y. Sun, J. Yang, Xa Li, Lead-free halide double perovskite materials: a new superstar toward green and stable optoelectronic applications, Nano-Micro Lett. 11 (2019) 1–18, https://doi.org/ 10.1007/s40820-019-0244-6.
- [8] L. Chu, W. Liu, Z. Qin, R. Zhang, R. Hu, J. Yang, J. Yang, Xa Li, Histamine H1 receptor gene polymorphism acts as a biological indicator of the prediction of therapeutic efficacy in patients with allergic rhinitis in the Chinese Han population, Sol. Energy Mater. Sol. Cells 178 (2018) 164–169, https://doi.org/10.1016/j.celmat.2018.01.010
- [9] S.D. Stranks, H.J. Snaith, Metal-halide perovskites for photovoltaic and lightemitting devices, Nat. Nanotechnol. 10 (2015) 391–402, https://doi.org/10.1038/ nnano.2015.90.

- [10] C.-C. Chueh, C.-Z. Li, A.K.-Y. Jen, Recent progress and perspective in solution-processed Interfacial materials for efficient and stable polymer and organometal perovskite solar cells, Energy Environ. Sci. 8 (2015) 1160–1189, https://doi.org/10.1039/C4EE03824J.
- [11] Y. Yang, F. Min, Y. Qiao, Z. Li, F. Vogelbacher, Z. Liu, W. Lv, Y. Wang, Y. Song, Embossed transparent electrodes assembled by bubble templates for efficient flexible perovskite solar cells, Nano Energy 89 (2021), 106384, https://doi.org/ 10.1016/j.nanoen.2021.106384.
- [12] J. Jeong, M. Kim, J. Seo, H. Lu, P. Ahlawat, A. Mishra, Y. Yang, M.A. Hope, F. T. Eickemeyer, M. Kim, Pseudo-halide anion engineering for α-FAPbl3 perovskite solar cells, Nature 592 (2021) 381–385, https://doi.org/10.1038/s41586-021-03406-5
- [13] E. Edri, S. Kirmayer, S. Mukhopadhyay, K. Gartsman, G. Hodes, D. Cahen, Elucidating the charge carrier separation and working mechanism of CH3NH3PbI3-xClx perovskite solar cells, Nat. Commun. 5 (2014) 1–8, https://doi.org/10.1038/ncomms4461.
- [14] V.W. Bergmann, S.A. Weber, F.J. Ramos, M.K. Nazeeruddin, M. Grätzel, D. Li, A. L. Domanski, I. Lieberwirth, S. Ahmad, R. Berger, Real-space observation of unbalanced charge distribution inside a perovskite-sensitized solar cell, Nat. Commun. 5 (2014) 1–9, https://doi.org/10.1038/ncomms6001.
- [15] H. Min, M. Kim, S.-U. Lee, H. Kim, G. Kim, K. Choi, J.H. Lee, S.I. Seok, Efficient, stable solar cells by using inherent bandgap of α-phase formamidinium lead iodide, Science 366 (2019) 749–753, https://doi.org/10.1126/science.aay7044.
- [16] L. Yan, Q. Xue, M. Liu, Z. Zhu, J. Tian, Z. Li, Z. Chen, Z. Chen, H. Yan, H.-L. Yip, Y. Cao, Interface engineering for all-inorganic CsPbI2Br perovskite solar cells with efficiency over 14, Adv. Mater. 30 (2018), 1802509, https://doi.org/10.1002/adms.201802509
- [17] K. Wang, C. Liu, P. Du, J. Zheng, X. Gong, Bulk heterojunction perovskite hybrid solar cells with large fill factor, Energy Environ. Sci. 8 (2015) 1245–1255, https://doi.org/10.1039/C5EE00222B.
- [18] C. Liu, K. Wang, P. Du, C. Yi, T. Meng, X. Gong, Efficient solution-processed bulk heterojunction perovskite hybrid solar cells, Adv. Energy Mater. 5 (2015), 1402024, https://doi.org/10.1002/aenm.201402024.
- [19] C.-H. Chiang, C.-G. Wu, Apparatus for comparison of pullout forces for various thoracic stent grafts at varying neck angulations and oversizes, Nat. Photonics 10 (2016) 196–200, https://doi.org/10.1038/nphoton.2016.3.
- [20] Y. Liu, Z. Hong, Q. Chen, W. Chang, H. Zhou, T.-B. Song, E. Young, Y. Yang, J. You, G. Li, Integrated perovskite/bulk-heterojunction toward efficient solar cells, Nano Lett. 15 (2015) 662–668, https://doi.org/10.1021/nl504168q.
- [21] J. Kim, G. Kim, H. Back, J. Kong, I.W. Hwang, T.K. Kim, S. Kwon, J.H. Lee, J. Lee, K. Yu, High-performance integrated perovskite and organic solar cells with enhanced fill factors and near-infrared harvesting, Adv. Mater. 28 (2016) 3159–3165. https://doi.org/10.1002/adma.201504555.
- [22] S. Dong, Y. Liu, Z. Hong, E. Yao, P. Sun, L. Meng, Y. Lin, J. Huang, G. Li, Y. Yang, Unraveling the high open circuit voltage and high performance of integrated perovskite/organic bulk-heterojunction solar cells, Nano Lett. 17 (2017) 5140–5147, https://doi.org/10.1021/acs.nanolett.7b02532.
- [23] R. Singh, V.K. Shukla, The validity and sensitivity of rheumatoid arthritis pain scale on a different ethnic group from indian rheumatoid arthritis patients, Sol. Energy 178 (2019) 90–97, https://doi.org/10.1016/j.solener.2018.12.014.
- [24] X. Zheng, J. Troughton, N. Gasparini, Y. Lin, M. Wei, Y. Hou, J. Liu, K. Song, Z. Chen, C. Yang, Low-intensity pulsed ultrasound attenuates cardiac inflammation of CVB3-induced viral myocarditis via regulation of caveolin-1 and MAPK pathways, Joule 3 (2019) 1963–1976, https://doi.org/10.1016/j.joule.2019.05.005.
- [25] W. Xu, L. Zheng, T. Zhu, L. Liu, X. Gong, Bulk heterojunction perovskite solar cells incorporated with Zn2SnO4 nanoparticles as the electron acceptors, ACS Appl. Mater. Interfaces 11 (2019) 34020–34029, https://doi.org/10.1021/ acsami.9b12346.
- [26] X. Gong, M. Tong, Y. Xia, W. Cai, J.S. Moon, Y. Cao, G. Yu, C.-L. Shieh, B. Nilsson, A.J. Heeger, High-detectivity polymer photodetectors with spectral response from 300 nm to 1450 nm, Science 325 (2009) 1665–1667, https://doi.org/10.1126/ science.1176706.
- [27] J. Huang, P. Xu, J. Liu, X.Z. You, Sequential introduction of cations deriving large-grain CsxFA1—xPbI3 thin film for planar hybrid solar cells: insight into phase-segregation and thermal-healing behavior, Small 13 (2017), 1603225, https://doi.org/10.1002/smll.201603225.
- [28] X. Xu, C. Ma, Y.-M. Xie, Y. Cheng, Y. Tian, M. Li, Y. Ma, C.-S. Lee, S.-W. Tsang, Air-processed mixed-cation Cs0.15FA0.85Pb13 planar perovskite solar cells derived from a Pb12-Cs1-FAI intermediate complex, J. Mater. Chem. A 6 (2018) 7731-7740, https://doi.org/10.1039/C8TA01049H.
- [29] J. Li, R. Yang, L. Que, Y. Wang, F. Wang, J. Wu, S. Li, Dissolution behavior of isolated and aggregated hematite particles revealed by in situ liquid cell transmission electron microscopy, J. Mater. Res. 34 (2019) 2416–2424, https:// doi.org/10.1557/jmr.2019.122.
- [30] W. Xu, Y. Gao, W. Ming, F. He, J. Li, X.H. Zhu, F. Kang, J. Li, G. Wei, Suppressing defects-induced nonradiative recombination for efficient perovskite solar cells through green antisolvent engineering, Adv. Mater. 32 (2020), 2003965, https:// doi.org/10.1002/adma.202003965.
- [31] T. Zhu, Y. Yang, S. Zhou, X. Yao, L. Liu, W. Hu, X. Gong, Structural basis for Ca²⁺-dependent activation of a plant metacaspase, Chin. Chem. Lett. 31 (2020) 2249–2253, https://doi.org/10.1016/j.cclet.2020.02.004.
- [32] R.H. Bube, Trap density determination by space-charge-limited currents, J. Appl. Phys. 33 (1962) 1733–1737, https://doi.org/10.1063/1.1728818.
- [33] V.M. Le Corre, E.A. Duijnstee, O. El Tambouli, J.M. Ball, H.J. Snaith, J. Lim, L.J. A. Koster, Revealing charge carrier mobility and defect densities in metal halide

- perovskites via space-charge-limited current measurements, ACS Energy Lett. 6 (3) (2021) 1087–1094, https://doi.org/10.1021/acsenergylett.0c02599.
- [34] P. Liu, W. Wang, S. Liu, H. Yang, Z. Shao, Fundamental understanding of photocurrent hysteresis in perovskite solar cells, Adv. Energy Mater. 9 (2019), 1803017, https://doi.org/10.1002/aenm.201803017.
- [35] H.J. Snaith, A. Abate, J.M. Ball, G.E. Eperon, T. Leijtens, N.K. Noel, S.D. Stranks, J. T.-W. Wang, K. Wojciechowski, W. Zhang, Anomalous hysteresis in perovskite solar cells, J. Phys. Chem. Lett. 5 (2014) 1511–1515, https://doi.org/10.1021/i2500113x.
- [36] J.H. Heo, H.J. Han, D. Kim, T.K. Ahn, S.H. Im, Hysteresis-less inverted CH3NH3Pbl3 planar perovskite hybrid solar cells with 18.1% power conversion efficiency, Energy Environ. Sci. 8 (2015) 1602–1608, https://doi.org/10.1039/ C5EP001201
- [37] W.S. Yang, B.-W. Park, E.H. Jung, N.J. Jeon, Y.C. Kim, D.U. Lee, S.S. Shin, J. Seo, E. K. Kim, J.H. Noh, S.I. Seok, Iodide management in formamidinium-lead-halide-based perovskite layers for efficient solar cells, Science 356 (2017) 1376–1379, https://doi.org/10.1126/science.aan2301.
- [38] C. Li, S. Tscheuschner, F. Paulus, P.E. Hopkinson, J. Kießling, A. Köhler, Y. Vaynzof, S. Huettner, Iodine migration and its effect on hysteresis in perovskite solar cells, Adv. Mater. 28 (2016) 2446–2454, https://doi.org/10.1002/ adm/201503232
- [39] F. Giordano, A. Abate, J.P.C. Baena, M. Saliba, T. Matsui, S.H. Im, S. M. Zakeeruddin, M.K. Nazeeruddin, A. Hagfeldt, M. Graetzel, Nat. Commun. 7 (2016) 1–6, https://doi.org/10.1038/ncomms10379.
- [40] H.-S. Kim, N.-G. Park, Parameters affecting I-V hysteresis of CH3NH3Pbl3 perovskite solar cells: effects of perovskite crystal size and mesoporous TiO2 layer, J. Phys. Chem. Lett. 5 (2014) 2927–2934, https://doi.org/10.1021/jz501392m.
- [41] K. Wang, L. Zheng, T. Zhu, X. Yao, C. Yi, X. Zhang, Y. Cao, L. Liu, W. Hu, X. Gong, Efficient perovskite solar cells by hybrid perovskites incorporated with heterovalent neodymium cations, Nano Energy 61 (2019) 352–360, https://doi. org/10.1016/j.nanoen.2019.04.073.
- [42] M. Zhou, J.S. Sarmiento, C. Fei, H. Wang, Charge transfer and diffusion at the perovskite/PCBM interface probed by transient absorption and reflection, J. Phys. Chem. C 123 (2019) 22095–22103, https://doi.org/10.1021/acs.jpcc.9b07591.
- [43] S. van Reenen, M. Kemerink, H.J. Snaith, Modeling anomalous hysteresis in perovskite solar cells, J. Phys. Chem. Lett. 6 (2015) 3808–3814, https://doi.org/ 10.1021/acs.ipclett.5b01645.
- [44] J. Seifter, Y. Sun, A.J. Heeger, Transient photocurrent response of small-molecule bulk heterojunction solar cells, Adv. Mater. 26 (2014) 2486–2493, https://doi.org/ 10.1002/adma.201305160.
- [45] K. Wang, L. Zheng, T. Zhu, L. Liu, M.L. Becker, X. Gong, High performance perovskites solar cells by hybrid perovskites co-crystallized with poly(ethylene oxide, Nano Energy 67 (2020), 104229, https://doi.org/10.1016/j. pangen_2019_104229.
- [46] T. Zhu, Y. Yang, K. Gu, C. Liu, J. Zheng, X. Gong, Novel quasi-2D perovskites for stable and efficient perovskite solar cells, ACS Appl. Mater. Interfaces 12 (2020) 51744–51755. https://doi.org/10.1021/acsami.0c16514.
- [47] R. Street, M. Schoendorf, A. Roy, J. Lee, Interface state recombination in organic solar cells, Phys. Rev. B 81 (2010), 205307, https://doi.org/10.1103/ PhysRevB.81.205307.

- [48] S.R. Cowan, A. Roy, A.J. Heeger, Recombination in polymer-fullerene bulk heterojunction solar cells, Phys. Rev. B 82 (2010), 245207, https://doi.org/ 10.1103/PhysRevB.82.245207.
- [49] W. Xu, X. Yao, T. Meng, K. Wang, F. Huang, X. Gong, Y. Cao, Perovskite hybrid solar cells with a fullerene derivative electron extraction layer, J. Mater. Chem. C 5 (2017) 4190–4197, https://doi.org/10.1039/C7TC00597K.
- [50] L.J.A. Koster, V.D. Mihailetchi, R. Ramaker, P.W. Blom, Light intensity dependence of open-circuit voltage of polymer: fullerene solar cells, Appl. Phys. Lett. 86 (2005), 123509, https://doi.org/10.1063/1.1889240.
- [51] T. Zhu, L. Zheng, Z. Xiao, X. Meng, L. Liu, L. Ding, X. Gong, Functionality of nonfullerene electron acceptors in ternary organic solar cells, Sol. RRL 3 (2019), 1900322, https://doi.org/10.1002/solr.201900322.
- [52] Z. Li, W. Wang, N.C. Greenham, C.R. McNeill, Influence of nanoparticle shape on charge transport and recombination in polymer/nanocrystal solar cells, Phys. Chem. Chem. Phys. 16 (2014) 25684–25693, https://doi.org/10.1039/ C4CD011118
- [53] V.D. Mihailetchi, J. Wildeman, P.W.M. Blom, Space-charge limited photocurrent, Phys. Rev. Lett. 94 (2005), 126602, https://doi.org/10.1103/ PhysRevLett 94 126602
- [54] A.K.K. Kyaw, D.H. Wang, V. Gupta, W.L. Leong, L. Ke, G.C. Bazan, A.J. Heeger, Intensity dependence of current-voltage characteristics and recombination in highefficiency solution-processed small-molecule solar cells, ACS Nano 7 (2013) 4569–4577, https://doi.org/10.1021/nn401267s.
- [55] W. Xu, Y. Guo, X. Zhang, L. Zheng, T. Zhu, D. Zhao, W. Hu, X. Gong, Room-temperature-operated ultrasensitive broadband photodetectors by perovskite incorporated with conjugated polymer and single-wall carbon nanotubes, Adv. Funct. Mater. 28 (2018), 1705541, https://doi.org/10.1002/adfm.201705541.
- [56] C. Eames, J.M. Frost, P.R. Barnes, B.C. O'regan, A. Walsh, M.S. Islam, Ionic transport in hybrid lead iodide perovskite solar cells, Nat. Commun. 6 (2015) 1–8, https://doi.org/10.1038/ncomms8497.
- [57] K. Miyano, M. Yanagida, N. Tripathi, Y. Shirai, Hysteresis, stability, and ion migration in lead halide perovskite photovoltaics, J. Phys. Chem. Lett. 7 (12) (2016) 2240–2245, https://doi.org/10.1021/acs.jpclett.6b00579.
- [58] S.M. Sze, Y. Li, K.K. Ng, Physics of Semiconductor Devices, John wiley & sons, 2021
- [59] G.J.A. Wetzelaer, M. Scheepers, A.M. Sempere, C. Momblona, J. Ávila, H.J. Bolink, Trap-assisted non-radiative recombination in organic-inorganic perovskite solar cells, Adv. Mater. 27 (2015) 1837–1841, https://doi.org/10.1002/ adma.201405372.
- [60] W.A. Laban, L. Etgar, Depleted hole conductor-free lead halide iodide heterojunction solar cells, Energy Environ. Sci. 6 (2013) 3249–3253, https://doi. org/10.1039/C3EE42282H.
- [61] P. Murgatroyd, Theory of space-charge-limited current enhanced by Frenkel effect, J. Phys. D: Appl. Phys. 3 (1970) 151–156, https://doi.org/10.1088/0022-3727/3/ 2/308.
- [62] Z. Jiang, X. Li, J. Strzalka, M. Sprung, T. Sun, A.R. Sandy, S. Narayanan, D.R. Lee, J. Wang, The dedicated high-resolution grazing-incidence X-ray scattering beamline 8-ID-E at the advanced photon source, J. Synchrotron Radiat. 19 (2012) 627–636, https://doi.org/10.1107/S0909049512022017.
- [63] W. Xu, L. Zheng, X. Zhang, Y. Cao, T. Meng, D. Wu, L. Liu, W. Hu, X. Gong, Efficient perovskite solar cells fabricated by co partially substituted hybrid perovskite, Adv. Energy Mater. 9 (2019), 1902152, https://doi.org/10.1002/aenm.201902152.